FERROELECTRICS

Emergent ferroelectricity in subnanometer binary oxide films on silicon

Suraj S. Cheema[1,2]*†, Nirmaan Shanker[2]†, Shang-Lin Hsu[2]†, Yoonsoo Rho[3], Cheng-Hsiang Hsu[2], Vladimir A. Stoica[4,5], Zhan Zhang[5], John W. Freeland[5], Padraic Shafer[6], Costas P. Grigoropoulos[3], Jim Ciston[7], Sayeef Salahuddin[2,8]*

The critical size limit of voltage-switchable electric dipoles has extensive implications for energy-efficient electronics, underlying the importance of ferroelectric order stabilized at reduced dimensionality. We report on the thickness-dependent antiferroelectric-to-ferroelectric phase transition in zirconium dioxide (ZrO_2) thin films on silicon. The emergent ferroelectricity and hysteretic polarization switching in ultrathin ZrO_2, conventionally a paraelectric material, notably persists down to a film thickness of 5 angstroms, the fluorite-structure unit-cell size. This approach to exploit three-dimensional centrosymmetric materials deposited down to the two-dimensional thickness limit, particularly within this model fluorite-structure system that possesses unconventional ferroelectric size effects, offers substantial promise for electronics, demonstrated by proof-of-principle atomic-scale nonvolatile ferroelectric memory on silicon. Additionally, it is also indicative of hidden electronic phenomena that are achievable across a wide class of simple binary materials.

The evolution of ferroic order at reduced dimensions—in particular, two-dimensional (2D) ferroelectricity—has long been intriguing for scaled energy-efficient electronics (*1*) because of the inherent ability to control electric polarization with an applied voltage (*2*). Since the discovery of ferroelectricity and antiferroelectricity in HfO_2-ZrO_2–based thin films (*3*, *4*), fluorite-structure binary oxides have reignited such interest (*5*) because they overcome many of the thickness-scaling (*6*, *7*) and silicon-compatibility issues (*8*) that afflict their perovskite and van der Waals ferroelectric counterparts. Early studies into fluorite-structure systems examined the ferroelectric-antiferroelectric phase competition in HfO_2-ZrO_2 solid solutions as a function of composition (*9*), typically in the 10-nm regime (*8*); meanwhile, recent works demonstrated ferroelectricity down to a sub-2-nm thickness in epitaxial (*10*) and polycrystalline (*11*) Zr:HfO_2 films.

Considering the implications of voltage-driven polarization switching for memory applications (*8*), the fundamental size limit of ferroelectric order in fluorite-structure systems is of critical importance. First-principles calculations have shown that 2D HfO_2 layers in their polar orthorhombic structure ($Pca2_1$) have minimal electrostatic penalty—that is, depolarizing field—enabling unsuppressed polarization down to the unit-cell limit (*12*, *13*). Furthermore, monolayer ZrO_2 was predicted to support switchable polarization on an atomically abrupt structure with Si (*14*). These predictions of scale-free fluorite-structure ferroelectricity (*12*, *14*) strongly motivate experimental demonstration of subnanometer polarization switching in this binary oxide system on silicon toward realizing highly scaled low-power nonvolatile memories (*8*, *12*).

Our strategy to achieve atomic-scale ferroelectricity aims to convert the conventionally antiferroelectric tetragonal phase (t-phase) of ZrO_2 (t-ZrO_2: $P4_2/nmc$) to the ferroelectric orthorhombic phase (o-phase) of ZrO_2 (o-ZrO_2: $Pca2_1$) through reduced dimensionality (Fig. 1A). The reduced dimensionality stabilizes the pressure-induced ferroelectric o-phase in fluorite-based oxides—conventionally achieved through hydrostatic pressure (*15*), chemical pressure (*9*), or epitaxial strain (*16*)—in the ultrathin regime, akin to size-driven antiferroelectric-to-ferroelectric phase transitions observed in prototypical perovskite ferroelectrics (*17*). We demonstrate the emergence of atomic-scale ferroelectricity in conventionally paraelectric ZrO_2 films down to a thickness of 5 Å, corresponding to the fluorite-structure unit-cell size.

ZrO_2 films with thicknesses from 10 nm to 5 Å (Fig. 1B), which we confirmed with synchrotron x-ray and transmission electron microscopy (TEM) analysis (figs. S1 and S2), are grown by atomic layer deposition on SiO_2-buffered Si (Fig. 1C) (*18*). To study the thickness-dependent antiferroelectric-ferroelectric evolution in ZrO_2, we examined the structural signatures of the respective t- and o-phases (Fig. 1). Synchrotron in-plane grazing incidence diffraction (IP-GID) spectra confirm the expected t-phase (101) reflection in thicker (3 to 10 nm) ZrO_2 films and the emergence of the o-phase (111) reflections for ultrathin (≤2 nm) films down to a thickness of 5 Å (Fig. 1B), concurrent with the emergence of highly oriented films (fig. S3) and supported by detailed IP-GID indexing (fig. S4) (*18*).

Distinguishing the nearly identical polar o-phase and nonpolar t-phase structural polymorphs can be further clarified by local oxygen atomic imaging (*19*, *20*). We used oxygen-sensitive negative spherical aberration imaging (*20*) and high-resolution TEM (HR-TEM) to identify the expected nonpolar t-phase in 5-nm ZrO_2 films (Fig. 1, D and E), aided by oxygen analysis (fig. S5) and HR-TEM simulations (fig. S6). Notably, this technique indicates that the polar o-phase emerges in 2-nm ZrO_2 films (Fig. 1, F and G), which x-ray analysis (Fig. 1B) pinpoints as the onset of ferroelectric o-ZrO_2 stabilization, as identified by its characteristic zigzag-like oxygen arrangement that is visible along the [110] projection (Fig. 1G). Additionally, lattice-angle analysis from traditional cation imaging matches $P4_2/nmc$ and $Pca2_1$ HR-TEM simulations for 5- and 2-nm ZrO_2 films, respectively (fig. S7), consistent with oxygen imaging.

To further examine this thickness-dependent antiferroelectric-to-ferroelectric transition, we used additional synchrotron x-ray studies to detect structural signatures of the respective ferroic phases (Fig. 2). From thickness-dependent GID, we found that the interplanar lattice spacing (o-d_{111} or t-d_{101}) and aspect ratio [$2c/(a+b)$ or c/a], which are structural barometers of lattice distortion established for fluorite-structure films (*18*), sharply rise at thicknesses less than 3 nm (Fig. 2A). These observations indicate increased polar o-ZrO_2 stabilization in the atomic-scale limit (Fig. 1B). Along with diffraction, x-ray spectroscopy provides another gauge of the fluorite-structure symmetry. Thickness-dependent x-ray absorption spectra at the oxygen *K*-edge (fig. S8) demonstrate larger crystal field splitting (Fig. 2B) below 3 nm, suggesting more pronounced polar distortion (*18*). Indeed, secondary crystal field splitting that arises from the polar rhombic distortion, a fingerprint of the ferroelectric o-phase (fig. S8), emerges for 5- and 10-Å ZrO_2. Furthermore, x-ray linear dichroism from zirconium $M_{3,2}$- and $L_{3,2}$-edges (fig. S8) indicates more pronounced orbital polarization, linked to electric polarization that arises from ferroelectric polar distortions (*11*, *18*), in the ultrathin regime (Fig. 2B). These thickness-dependent diffraction and spectroscopy trends support the ultrathin-amplified emergence of ferroelectric o-ZrO_2 in typically antiferroelectric t-ZrO_2 films.

Optical microscopy observations also support the size-dependent ferroic phase evolution,

[1]Department of Materials Science and Engineering, University of California, Berkeley, CA, USA. [2]Department of Electrical Engineering and Computer Sciences, University of California, Berkeley, CA, USA. [3]Laser Thermal Laboratory, Department of Mechanical Engineering, University of California, Berkeley, CA, USA. [4]Department of Materials Science and Engineering, Pennsylvania State University, University Park, PA, USA. [5]Advanced Photon Source, Argonne National Laboratory, Lemont, IL, USA. [6]Advanced Light Source, Lawrence Berkeley National Laboratory, Berkeley, CA, USA. [7]National Center for Electron Microscopy, Molecular Foundry, Lawrence Berkeley National Laboratory, Berkeley, CA, USA. [8]Materials Sciences Division, Lawrence Berkeley National Laboratory, Berkeley, CA, USA.
*Corresponding author. Email: s.cheema@berkeley.edu (S.S.C.); sayeef@berkeley.edu (S.S.)
†These authors contributed equally to this work.

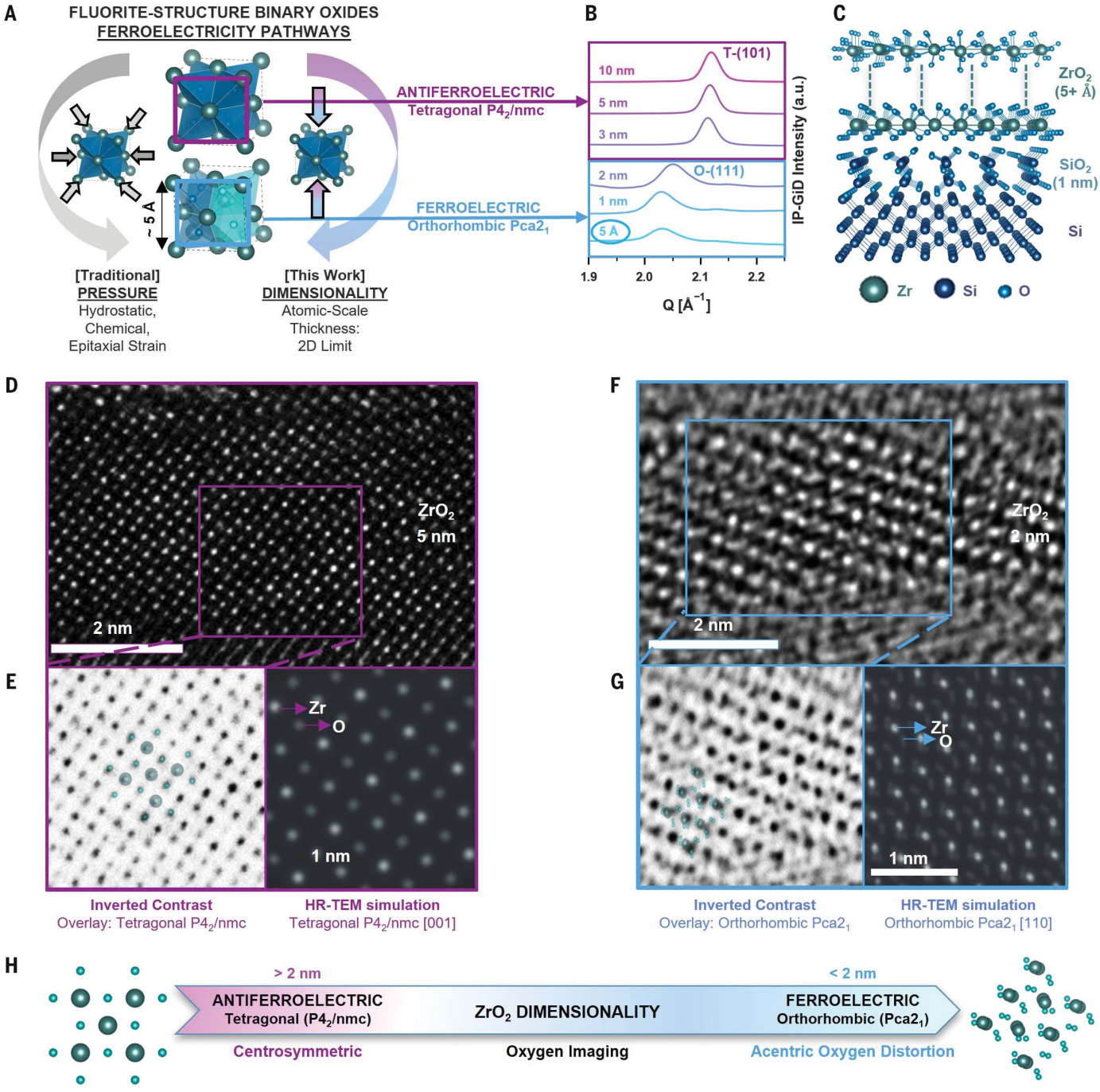

Fig. 1. Atomic-scale emergence of ferroelectricity in ZrO_2. (**A**) Pressure-driven pathways to ferroelectricity in fluorite-structure binary oxides; dimensionality—that is, atomic-scale thickness scaling—can induce ferroelectric o-ZrO_2 stabilization in conventionally antiferroelectric t-ZrO_2. (**B**) Thickness-dependent IP-GID demonstrating the tetragonal-to-orthorhombic phase transition in the ultrathin (5 Å to 2 nm) regime (fig. S4). a.u., arbitrary units; Q, scattering vector. (**C**) Schematic of the Si/SiO_2(1 nm)/ZrO_2(0.5 to 10 nm) films grown by atomic layer deposition. (**D** to **G**) Cross-sectional HR-TEM images of 5-nm ZrO_2 (D) and 2-nm ZrO_2 (F) indexed by oxygen-sensitive negative spherical aberration imaging and inverted contrast HR-TEM simulations (figs. S5 and S6), fit to the t-phase (E) and o-phase (G) lattice along the [001] and [110] zone axes, respectively. For inverted contrast images [(E) and (G)], light (dark) atoms represent O (Zr) atoms. Note the faint zigzag oxygen arrangements expected for the o-phase [110] projection (G). (**H**) Dimensionality-driven antiferroelectric-to-ferroelectric evolution of ZrO_2 demonstrated through oxygen imaging, sensitive to the anion distortion present in fluorite-structure binary oxides.

because the increase in the second-harmonic generation (SHG) signal, which is related to macroscopic polarization (*18*), with decreasing ZrO_2 thickness (Fig. 2C) is consistent with the ultrathin-enhanced polar distortion trends. Additionally, thickness-dependent capacitance-voltage (*C-V*) measurements of metal-oxide-semiconductor capacitors (fig. S9) indicate a crossover from an antiferroelectric-like t-phase permittivity (κ), κ ~ 40 (*4*), toward a more ferroelectric-like o-phase permittivity, κ ~ 30 (*4*, *21*), for ultrathin ZrO_2 films, again consistent with structural characterization.

To further characterize the electrical behavior, we fabricated metal-insulator-metal (MIM)

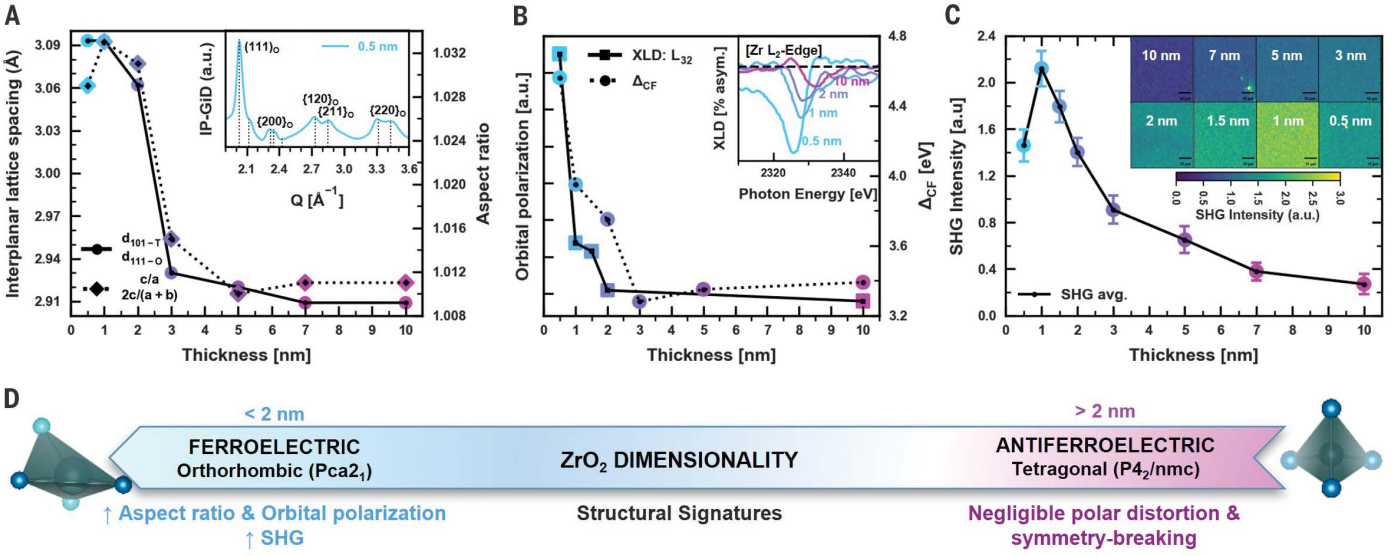

Fig. 2. Thickness-dependent ferroic phase evolution in ultrathin ZrO_2. (**A**) Thickness-dependent lattice spacing (t-d_{101} or o-d_{111}; solid line; left *y* axis) and aspect ratio (t-phase *c*/*a* or o-phase 2*c*/(*a* + *b*); dashed line; right *y* axis) indicating ultrathin-enhanced lattice distortion. The inset shows example IP-GID spectra for 0.5-nm ZrO_2 indexed to the ferroelectric o-phase. The structural markers for ultrathin (0.5 to 2 nm) and thicker (3 to 10 nm) ZrO_2 films are extracted from IP-GID spectra (fig. S4) and OOP-GID spectra, respectively (*18*). (**B**) Thickness-dependent crystal-field splitting (O *K*-edge x-ray absorption spectra; solid line; left *y* axis) and orbital polarization (Zr-$L_{3,2}$-edge x-ray linear dichroism (XLD); dashed line; right *y* axis) indicating ultrathin-amplified structural and polar distortion (*18*) (fig. S8). The inset shows an increase in orbital polarization at the Zr-L_2-edge with decreasing ZrO_2 thickness. Δ_{CF}, crystal field distortion. (**C**) Averaged SHG intensity of bare ZrO_2 films (0.5 to 10 nm) increases with decreasing ZrO_2 thickness, indicative of ultrathin-enhanced remnant polarization. The inset shows 2D SHG maps for the entire ZrO_2 thickness series. Further evidence of strong (weak) SHG intensity in ultrathin polar (thick nonpolar) ZrO_2 samples is provided by SHG spectra (fig. S11). (**D**) Dimensionality-driven antiferroelectric-to-ferroelectric evolution of ZrO_2 demonstrated through various structural signatures.

capacitors with varying ZrO_2 thicknesses (Fig. 3A). Considering that antiferroelectrics are defined based on their field-induced transition to a proximal polar phase and not simply their parent crystal structure (*17*), voltage-dependent hysteretic behavior is required to probe the underlying ferroic order, beyond crystallographic signatures of their parent structure. MIM polarization-voltage (*P-V*) loops for 5- and 10-nm-thick ZrO_2, the typical t-ZrO_2 thickness regime (*4*, *8*), demonstrate a signature antiferroelectric-like double hysteresis (*17*) (Fig. 3B). Importantly, conventional *P-V* probes of the signature behavior cannot be applied to the ultrathin regime (*18*), in which nonpolarization-dependent leakage current masks polarization-dependent switching current.

To directly probe the polarization switching properties of ultrathin ZrO_2 films while suppressing leakage current, we fabricated interdigitated electrodes (IDEs) to facilitate in-plane (IP) polarization switching (Fig. 3D). In IDE structures, leakage is no longer limited by the ZrO_2 thickness (~5 Å to 10 nm) but rather by the IP electrode spacing (~1 μm). The expected field-induced nonpolar-to-polar phase transition for fluorite-structure antiferroelectrics (*8*, *18*), illustrated by double-switching *P-V* behavior in the IDE structures, is observed for thick (5 and 10 nm) t-ZrO_2 films (Fig. 3E and fig. S10). As ZrO_2 drops below the critical 2-nm thickness, *P-V* behavior for 1-nm and 5-Å ZrO_2 displays ferroelectric-like counterclockwise polarization switching (Fig. 3F and fig. S10). The polarization switching in this IP geometry is consistent with SHG imaging (Fig. 2C) and SHG spectra (fig. S11), whose geometry (fig. S12) is sensitive to IP inversion symmetry breaking (*18*) rather than out-of-plane (OOP) inversion symmetry breaking mapped by piezoresponse force microscopy imaging (fig. S13).

Pulsed current-voltage (*I-V*) measurements in metal-ferroelectric-insulator-semiconductor (MFIS) tunnel junction structures (Fig. 3C) provide additional ferroic phase insights into ZrO_2, in which tunnel electroresistance reflects the ferroelectric polarization evolution with field (*18*). For ultrathin (1 and 0.5 nm) ZrO_2 tunnel barriers (Fig. 3C), abrupt bistable resistance states exhibit counterclockwise hysteresis, consistent with ferroelectric polarization switching in the MFIS geometry and voltage polarity–independent hysteretic behavior (fig. S14). Similar tunnel electroresistance hysteresis maps have been shown for ferroelectric tunnel junctions that integrate ultrathin Zr:HfO_2 barriers (*11*, *22*, *23*), but until this point, fluorite-based ferroelectric tunnel junctions have not been demonstrated below 1 nm.

To unravel these anomalous size effects, specifically the emergent 2D ferroelectricity in a conventionally paraelectric material, surface energies, which take on an amplified role in the ultrasmall and ultrathin regime (*21*), can provide key insights into fluorite polymorphic phase stability (*15*). First-principles calculations that consider surface-energy contributions predict lower o-phase Gibbs free energy relative to the t-phase at ultrasmall sizes (<4 nm) and large pressures for the HfO_2-ZrO_2 system (*21*). Indeed, pressure-driven stabilization of the o-phase in ZrO_2 has been observed through hydrostatic pressure in bulk ZrO_2 (*15*) and epitaxial strain in thin-film ZrO_2 (*16*, *24*). Here, 2D thickness scaling—that is, confinement in the vertical dimension (Fig. 1A)—should trigger similar pressure-driven and surface energy–induced effects. Accordingly, the ferroelectric o-phase is stabilized at reduced dimensions, as expected for ultrasmall crystallite sizes (*20*) and nanoscale grain sizes (*21*) in fluorite binary oxides. On the other hand, similar size effects typically destabilize the polar crystal structure in the conventional perovskite ferroelectrics (*25*), marking one key distinction between the two ferroelectric systems.

Besides simply stabilizing atomic-scale ferroelectricity, another puzzling feature lies in

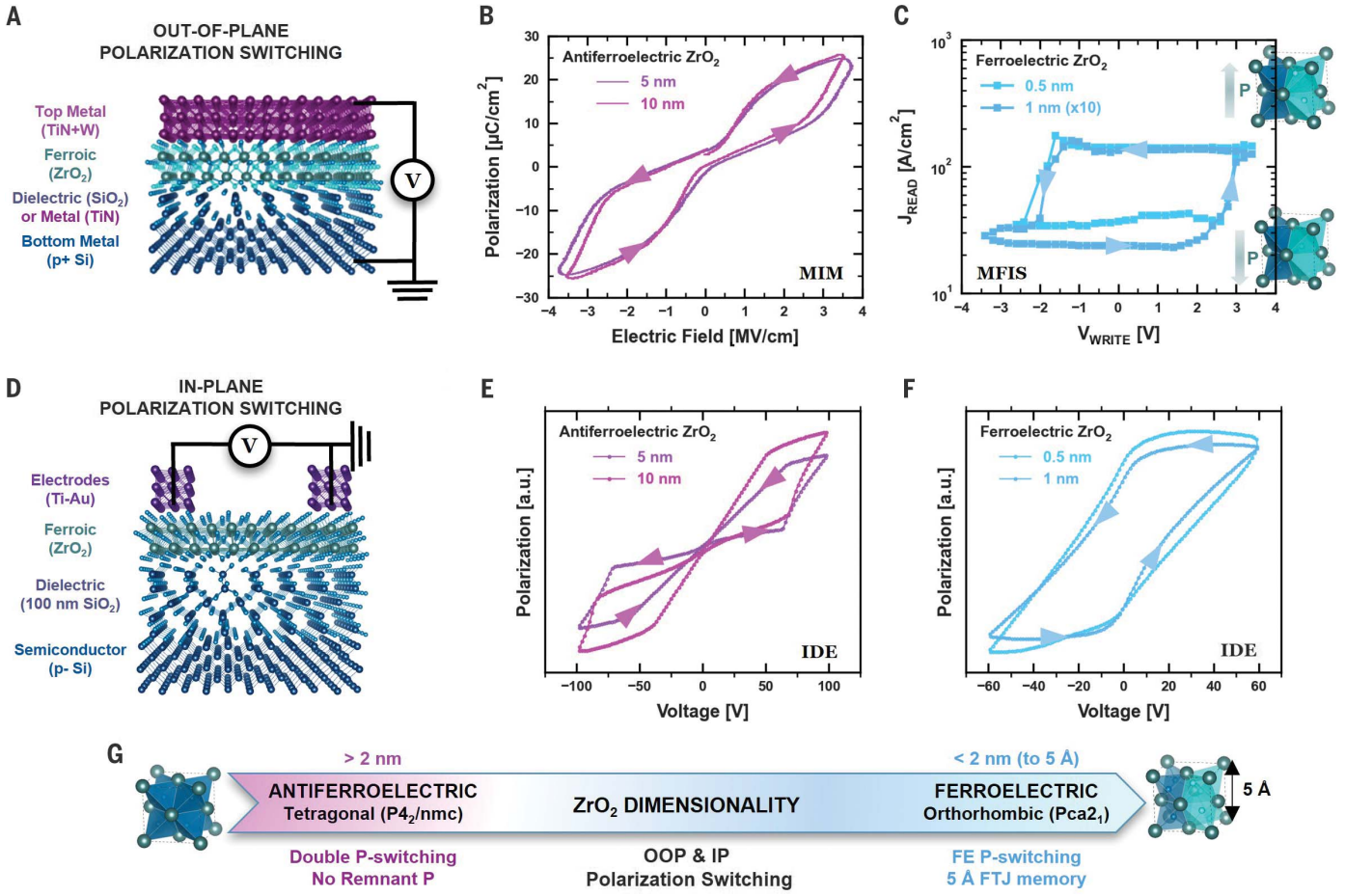

Fig. 3. Thickness-dependent polarization switching in ultrathin ZrO_2. (**A**) Schematic OOP capacitor geometries—MIM capacitors with bottom TiN and MFIS tunnel junctions with SiO_2 interlayer dielectrics—used to investigate thickness-dependent OOP polarization switching in ZrO_2. (**B**) Antiferroelectric-like OOP polarization switching observed in relatively thick (5 and 10 nm) ZrO_2 from MIM *P-V* hysteresis loops. (**C**) Ferroelectric-like OOP polarization switching observed in ultrathin (5 Å and 1 nm) ZrO_2 from pulsed *I-V* hysteresis loops measured in MFIS tunnel junctions, demonstrating two bistable remnant resistive states, consistent with ferroelectric polarization switching and piezoresponse force microscopy hysteresis loops (fig. S14). J_{READ}, read current; V_{WRITE}, write voltage. (**D**) Schematic IP device geometry (IDEs) used to investigate thickness-dependent IP polarization switching in ZrO_2. (**E** and **F**) Antiferroelectric-like (E) and ferroelectric-like (F) IP polarization switching observed in relatively thick (5 and 10 nm) ZrO_2 and ultrathin (5 Å and 1 nm) ZrO_2, respectively, from IDE *P-V* hysteresis loops. (**G**) Dimensionality-driven antiferroelectric-to-ferroelectric evolution of ZrO_2 demonstrated through OOP and IP polarization switching. FE, ferroelectric.

the amplified markers of polar distortion with decreased thickness (Fig. 2). Indeed, ZrO_2 demonstrates many of the same ultrathin-enhanced lattice distortion signatures as ferroelectric polycrystalline Zr:HfO_2 (*11*) and epitaxial Zr:HfO_2 (*10*, *26*) films. Therefore, these "reverse" size effects relative to its perovskite counterparts, in which polarization typically decreases with decreasing thickness (*7*), may be intrinsic to fluorites. Recent first-principles calculations indicate that the fluorite-structure o-phase ($Pca2_1$) displays a negative longitudinal piezoelectric effect (*27*), in which compression along the polarization direction leads to a larger polar distortion. Therefore, the negative longitudinal piezoelectric effect could provide an atomic-scale mechanism underlying the observed increased polar distortion as thickness is reduced to the ultrathin regime (*10*, *11*, *26*) in fluorite-structure ferroelectrics. This would mark another distinguishing feature from prototypical perovskite-based ferroelectric thin films, which demonstrate positive longitudinal piezoelectricity and diminished polar distortion at the atomic scale (*7*).

Along with the distinct piezoelectric origins (*27*), unconventional ferroelectric origins have also been attributed to fluorite-structure binary oxides (*12*, *13*). First-principles calculations suggest that 2D fluorite-structure $Pca2_1$ slabs maintain switchable polarization because of their improper nature (*12*); indeed, for improper ferroelectric transitions, the primary nonpolar structural distortion, from which the spontaneous polarization indirectly arises, is impervious to electrostatic depolarization effects (*28*). Therefore, improper fluorite ferroelectrics should display robust, switchable electric dipoles with no critical thickness (*12*), as we observed for ultrathin ZrO_2 (Fig. 3).

In addition to the depolarization-resistant nature of fluorite ferroelectricity (*12*, *13*), IP polarization can also help mitigate depolarization fields, which typically suppress OOP polarization in the ultrathin regime (*29*). Indeed, the ultrathin o-ZrO_2 films demonstrate IP polarization, as evidenced by IP inversion symmetry breaking (Fig. 2C) and polarization switching (Fig. 3F). These films exhibit predominant (111) OOP texture (Fig. 2A and fig. S3); considering that the $Pca2_1$ unit-cell polar axis lies along a principal lattice direction, o-ZrO_2 films project a substantial IP polarization. Therefore, the highly

oriented nature of the ultrathin ZrO_2 films, preferentially stacked along their close-packed (111) planes favored by surface-energy considerations, can also contribute to the sustained atomic-scale polarization.

Considering that traditional 3D materials may possess unrealized spontaneous polarization, exemplified here by a conventionally paraelectric binary oxide developing ferroelectric order at reduced dimensions, simply scaling the thickness to the atomic scale offers a straightforward, yet effective, route to 2D ferroelectricity by design in intrinsically centrosymmetric materials. Therefore, reduced dimensionality offers a powerful inversion symmetry–breaking methodology (*30*), along with epitaxial strain (*31*, *32*) and twisted heterostructures (*33*), for materials in proximity to pressure-induced polar instabilities, such as other simple binary oxides (*34*).

Specifically regarding the HfO_2-ZrO_2 binary oxide family, the emergence of atomic-scale ferroelectricity in ZrO_2 underscores the distinct nature of fluorite-structure size effects, in which reduced dimensionality induces ferroelectric order even in its conventionally antiferroelectric endmember, not just Zr:HfO_2 (*11*). Therefore, thickness-scaling alone can span the fluorite ferroelectric-antiferroelectric phase diagram, moving beyond the established HfO_2-ZrO_2 composition space (*4*, *8*, *9*). Furthermore, the observed polarization switching (Fig. 3) to the fluorite-structure unit-cell size, 5 Å, validates recent predictions of its unorthodox ferroelectric origins (*12*, *13*), likely marking the thinnest demonstration of hysteretic polarization switching in any ferroelectric system (table S1). Critically, the polarization switching for 5-Å ZrO_2 persists beyond 125°C (fig. S15), which is promising for electronic applications, such as nonvolatile ferroelectric memory (Fig. 3C). Therefore, simple fluorite-structure binary oxides offer a model material system not just to explore unconventional piezoelectric and ferroelectric phenomena at the 2D limit but also for integration into highly scaled next-generation Si electronics.

REFERENCES AND NOTES

1. S. Salahuddin, K. Ni, S. Datta, *Nat. Electron.* **1**, 442–450 (2018).
2. M. Dawber, K. M. Rabe, J. F. Scott, *Rev. Mod. Phys.* **77**, 1083–1130 (2005).
3. T. S. Böscke, J. Müller, D. Bräuhaus, U. Schröder, U. Böttger, *Appl. Phys. Lett.* **99**, 102903 (2011).
4. J. Müller *et al.*, *Nano Lett.* **12**, 4318–4323 (2012).
5. T. Mikolajick, U. Schroeder, M. H. Park, *Appl. Phys. Lett.* **118**, 180402 (2021).
6. H. Qiao, C. Wang, W. S. Choi, M. H. Park, Y. Kim, *Mater. Sci. Eng. Rep.* **145**, 100622 (2021).
7. J. F. Ihlefeld *et al.*, *J. Am. Ceram. Soc.* **99**, 2537–2557 (2016).
8. T. Mikolajick *et al.*, *J. Appl. Phys.* **129**, 100901 (2021).
9. U. Schroeder *et al.*, *Jpn. J. Appl. Phys.* **58**, SL0801 (2019).
10. Y. Wei *et al.*, *Nat. Mater.* **17**, 1095–1100 (2018).
11. S. S. Cheema *et al.*, *Nature* **580**, 478–482 (2020).
12. H.-J. Lee *et al.*, *Science* **369**, 1343–1347 (2020).
13. B. Noheda, J. Íñiguez, *Science* **369**, 1300–1301 (2020).
14. M. Dogan *et al.*, *Nano Lett.* **18**, 241–246 (2018).
15. O. Ohtaka *et al.*, *Phys. Rev. B* **63**, 174108 (2001).
16. T. Song *et al.*, *ACS Appl. Electron. Mater.* **3**, 2106–2113 (2021).
17. C. A. Randall, Z. Fan, I. Reaney, L. Chen, S. Trolier-McKinstry, *J. Am. Ceram. Soc.* **104**, 3775–3810 (2021).
18. Materials, methods, and additional information are available as supplementary materials.
19. P. Nukala *et al.*, *Science* **372**, 630–635 (2021).
20. H. Du *et al.*, *Matter* **4**, 986–1000 (2021).
21. R. Materlik, C. Künneth, A. Kersch, *J. Appl. Phys.* **117**, 134109 (2015).
22. Y. Wei *et al.*, *Phys. Rev. Appl.* **12**, 031001 (2019).
23. S. S. Cheema *et al.*, *Adv. Electron. Mater.* 10.1002/aelm.202100499 (2021).
24. S. E. Reyes-Lillo, K. F. Garrity, K. M. Rabe, *Phys. Rev. B* **90**, 140103 (2014).
25. W. J. Merz, *Phys. Rev.* **78**, 52–54 (1950).
26. J. Lyu, I. Fina, R. Solanas, J. Fontcuberta, F. Sánchez, *ACS Appl. Electron. Mater.* **1**, 220–228 (2019).
27. J. Liu, S. Liu, J.-Y. Yang, L. Liu, *Phys. Rev. Lett.* **125**, 197601 (2020).
28. N. Sai, C. J. Fennie, A. A. Demkov, *Phys. Rev. Lett.* **102**, 107601 (2009).
29. J. Junquera, P. Ghosez, *Nature* **422**, 506–509 (2003).
30. D. Lee *et al.*, *Science* **349**, 1314–1317 (2015).
31. M. P. Warusawithana *et al.*, *Science* **324**, 367–370 (2009).
32. J. H. Haeni *et al.*, *Nature* **430**, 758–761 (2004).
33. E. Tsymbal, *Science* **372**, 1389–1390 (2021).
34. R. Batra *et al.*, *Chem. Mater.* **32**, 3823–3832 (2020).

ACKNOWLEDGMENTS

S.S.C. and N.S. thank C. Tassone, A. Mehta, and K. Stone for experimental support at the Stanford Synchrotron Radiation Lightsource (SSRL) and R. Ramesh for access to scanning probe microscopy. **Funding:** This research was supported in part by the following: the Berkeley Center for Negative Capacitance Transistors (BCNCT); Applications and Systems-Driven Center for Energy-Efficient Integrated NanoTechnologies (ASCENT), one of the six centers in the Joint University Microelectronics Program (JUMP) initiative, a Semiconductor Research Corporation (SRC) program sponsored by Defense Advanced Research Projects Agency (DARPA); the DARPA Foundations Required for Novel Compute (FRANC) program; the Interaction of Ionizing Radiation with Matter (IIRM) University Research Alliance supported by the Department of Defense; and the US Department of Energy (DOE), Office of Science, Office of Basic Energy Sciences, Materials Sciences and Engineering Division, under contract no. DE-AC02-05-CH11231 (Microelectronics Co-Design program) for the development of materials for low-power microelectronics. This research used resources of the Advanced Photon Source (APS), a DOE Office of Science user facility operated for the DOE Office of Science by Argonne National Laboratory under contract no. DE-AC02-06CH11357. V.A.S. and J.W.F. were supported by the DOE, Office of Science, Basic Energy Sciences, under award no. DE-SC-0012375. Use of the SSRL, SLAC National Accelerator Laboratory, is supported by the DOE, Office of Science, Office of Basic Energy Sciences, under contract no. DE-AC0276SF00515. This research used resources of the Advanced Light Source (ALS), which is a DOE Office of Science User Facility under contract no. DE-AC02-05CH11231. Electron microscopy was performed at the Molecular Foundry, Lawrence Berkeley National Laboratory, supported by the DOE, Office of Science, Office of Basic Energy Sciences (DE-AC02-05CH11231). **Author contributions:** S.S.C. conceived the project and designed the research and experiments. S.S.C. performed film synthesis and ferroic phase optimization. N.S. performed device fabrication. N.S. and S.S.C. performed dielectric and electrical measurements. N.S. performed scanning probe microscopy with the supervision of J.C. S.-L.H. performed transmission electron microscopy and analysis. Y.R. performed second-harmonic generation with the supervision of C.P.G. S.S.C., C.-H.H., P.S., V.A.S., and J.W.F. performed synchrotron spectroscopy (at ALS and APS). S.S.C., N.S., V.A.S., and Z.Z. performed synchrotron diffraction (at SSRL and APS). S.S.C. wrote the manuscript. S.S.C., N.S., and S.S. edited the manuscript. S.S. supervised the research. **Competing interests:** The authors declare that they have no competing interests. **Data and materials availability:** All data are available in the manuscript or the supplementary materials.

SUPPLEMENTARY MATERIALS

science.org/doi/10.1126/science.abm8642
Materials and Methods
Supplementary Text
Figs. S1 to S15
Table S1
References (*35–132*)

Submitted 18 October 2021; resubmitted 14 February 2022
Accepted 1 April 2022
10.1126/science.abm8642

Science

Emergent ferroelectricity in subnanometer binary oxide films on silicon

Suraj S. CheemaNirmaan ShankerShang-Lin HsuYoonsoo RhoCheng-Hsiang HsuVladimir A. StoicaZhan ZhangJohn W. FreelandPadraic ShaferCostas P. GrigoropoulosJim CistonSayeef Salahuddin

Science, 376 (6593), • DOI: 10.1126/science.abm8642

Ultrathin ferroelectric films

The electrical properties of ferroelectrics can be changed with an electric field, making them attractive materials for computer hardware applications. Cheema *et al*. show that extremely thin films of zirconium dioxide on a silica substrate have ferroelectric order down to the unit cell scale. Whereas in many other materials the ferroelectric behavior is suppressed at the few-nanometer scale, a ferroelectric phase transition occurs if zirconium dioxide is thinner than two nanometers. This property might be true for any fluorite-structured binary oxide, making these types of thin films attractive for next-generation electronics. —BG

Science (ISSN) is published by the American Association for the Advancement of Science. 1200 New York Avenue NW, Washington, DC 20005. The title *Science* is a registered trademark of AAAS.